ELSEVIER

Journal of Fluids and Structures 26 (2010) 1174–1194

JOURNAL OF FLUIDS AND STRUCTURES

www.elsevier.com/locate/jfs

Aerodynamics of laminar separation flutter at a transitional Reynolds number

D. Poirel[a,*], W. Yuan[b]

[a]*Department of Mechanical Engineering, Royal Military College of Canada (RMC), PO Box 17000, Station Forces, Kingston, Ontario, Canada K7K 7B4*

[b]*Institute for Aerospace Research, National Research Council Canada (NRC), Ottawa, Ontario, Canada K1A 0R6*

Received 23 July 2009; accepted 13 June 2010
Available online 20 October 2010

Abstract

Experimental observations of self-sustained pitch oscillations of a NACA 0012 airfoil at transitional Reynolds numbers were recently reported. The aeroelastic limit cycle oscillations, herein labelled as *laminar separation flutter*, occur in the range $5.0 \times 10^4 \leq \mathrm{Re}_c \leq 1.3 \times 10^5$. They are well behaved, have a small amplitude and oscillate about $\theta = 0^\circ$. It has been speculated that laminar separation leading to the formation of a laminar separation bubble, occurring at these Reynolds numbers, plays an essential role in these oscillations. This paper focuses on the $\mathrm{Re}_c = 7.7 \times 10^4$ case, with the elastic axis located at 18.6% chord. Considering that the experimental rig acts as a dynamic balance, the aerodynamic moment is derived and is empirically modelled as a generalized Duffing–van-der-Pol nonlinearity. As expected, it behaves nonlinearly with pitch displacement and rate. It also indicates a dynamically unstable equilibrium point, i.e. negative aerodynamic damping. In addition, large eddy simulations of the flow around the airfoil undergoing prescribed simple harmonic motion, using the same amplitude and frequency as the aeroelastic oscillations, are performed. The comparison between the experiment and simulations is conclusive. Both approaches show that the work done by the airflow on the airfoil is positive and both have the same magnitude. The large eddy simulation (LES) computations indicate that at $\theta = 0^\circ$, the pitching motion induces a lag in the separation point on both surfaces of the airfoil resulting in negative pitching moment when pitching down, and positive moment when pitching up, thus feeding the LCO.

Keywords: Self-sustained oscillations; LCO; Low Re aerodynamics; Transitional boundary layer; Negative aerodynamic damping; Flutter

1. Introduction

Flows in the range of Reynolds numbers, $10^4 \leq \mathrm{Re}_c \leq 10^6$, exhibit complex viscous phenomena such as laminar boundary layer separation leading to the formation of a laminar separation bubble (LSB), via transition of the laminar shear layer and subsequent re-attachment of the turbulent layer (Gad-el-Hak, 1990; Mueller, 1985). On a lifting body, this peculiar flow physics manifests itself as a strongly nonlinear relationship between aerodynamic loads and angle of

*Corresponding author. Tel.: +1 613 541 6000x6452; fax: +1 613 542 8612.
E-mail address: poirel-d@rmc.ca (D. Poirel).

0889-9746/$ - see front matter
doi:10.1016/j.jfluidstructs.2010.06.005

Nomenclature

AR	aspect ratio of the model wing, s/c
c	airfoil chord length (m)
C_f	skin-friction coefficient, $\tau_w/(\frac{1}{2}\rho U^2)$
C_L	lift coefficient, $L/(\frac{1}{2}\rho U^2 sc)$
C_{Mea}	aerodynamic moment coefficient about the elastic axis, nose-up positive, $M_{\mathrm{EA}}/(\frac{1}{2}\rho U^2 sc^2)$
C_p	pressure coefficient $(p-p_\infty)/(\frac{1}{2}\rho U^2)$
D_s	viscous damping coefficient (N m s)
f	frequency (Hz)
f_s	natural structural frequency (Hz)
f_c	filter cut-off frequency (Hz)
I_s	mass moment of inertia of rotating parts about elastic axis (kg m^2)
k	reduced frequency, $\omega c/2U$
K_s	structural stiffness coefficient (N m)
m_θ	mass of parts in rotation (kg)
M_{EA}	aerodynamic moment about the elastic axis (N m)
Re_c	Reynolds number based on airfoil chord
s	wing span (m)
St_T	Strouhal number based on airfoil thickness, $f\,T/U$ (cycle)
Tu	free-stream turbulence intensity, u'_{rms}/U
U, U_∞	free-stream airspeed (m/s)
u	unsteady longitudinal flow velocity (m/s)
v	unsteady vertical flow velocity (m/s)
u'	unsteady longitudinal flow velocity fluctuation (m/s)
v'	unsteady vertical flow velocity fluctuation (m/s)
W_{aero}	work done by the aerodynamic moment (N m)
x	chordwise position (m)
α	angle of attack (deg)
Δx^+, Δy^+, Δz^+	grid size normalized by friction velocity
θ	pitch angle (deg or rad)
μ	airfoil/air mass ratio, $m_\theta/(\pi\rho s(c/2)^2)$

attack (AOA), even for very small angles well below stall (Gad-el-Hak, 1990; Mueller, 1985; Lutz et al., 2001; Huang et al., 1996; Huang and Lee, 1999). For instance, Fig. 1 shows the nonlinear static pitching moment coefficients of a NACA 0012 wing for two moderately low-Re numbers. These moments are reproduced from Huang et al. (1996). Note that the moment coefficients actually published in Huang et al. (1996) are an order of magnitude too large; this error was confirmed via e-mail (2006). Surface-oil flow analysis indicated laminar separation at angles of attack from 0° to 2° followed by a LSB between 2° and 13° approximately, the bubble moving forward with increase of angle of attack (Huang and Lee, 1999). Turbulent trailing-edge separation occurring aft of the LSB for angles above 8° was also observed.

This nonlinear behaviour is in direct contrast to high-Re flows for which lift and aerodynamic moment coefficients vary linearly with AOA, generally up to 10–12°. The richness and complexity of these low-Re flows have therefore the potential to significantly impact the aeroelastic dynamics. Experiments conducted on a rigid but flexibly held NACA 0012 airfoil, and reported in Poirel and Harris (2005), Poirel et al. (2006, 2008), showed self-sustained pitching oscillations in this range of Reynolds numbers. In addition, the oscillations were sensitive to the surface roughness and free-stream turbulence intensity. These observations suggested that the boundary layer transition played a significant role in the airfoil oscillations. It was hypothesized that they originate from a nonlinear coupling between the free pitching airfoil and the low-to-moderate transitional Re flows, the fundamental supporting evidence being that no

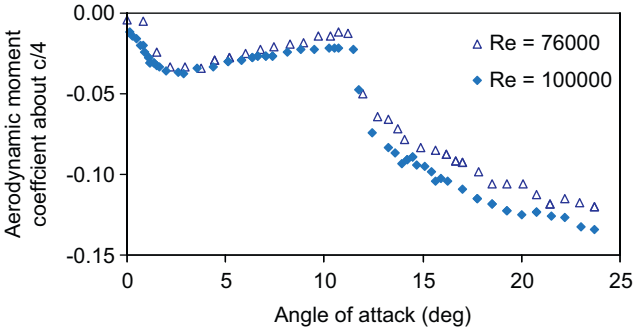

Fig. 1. Static aerodynamic moment coefficients about $c/4$. NACA 0012 wing, one end plate, AR = 5, Tu~0.2%. Reproduced in part (and corrected) from Fig. 12 of Huang et al. (1996).

periodicity in the free-stream, nor anywhere in the flow field around and in the wake of the fixed airfoil, could account for this behaviour. Furthermore, it was speculated that laminar trailing-edge separation and the presence of a laminar separation bubble played a crucial role. In particular, it was suggested that the oscillations are somehow initiated by laminar trailing-edge separation when initial conditions are close to 0°, whereas the steady state limit cycle is associated with the presence of a laminar separation bubble. Subsequent in-house flow visualizations of the airfoil statically held, using a fluorescent oil, showed laminar trailing-edge separation without re-attachment (i.e. open separation) at AOA $= 0^\circ$ followed by re-attachment (i.e. LSB) at slightly higher angles (Collin, 2007). These static tests corroborate Huang and Lee's (1999) findings. The physical mechanism at play for re-attachment is the separated shear layer which transitions to a turbulent state prior to reaching the trailing edge. Hence, as the angle of attack is increased, the laminar separation point moves up-stream and enables the separated shear layer to re-attach downstream after it has transitioned from laminar to turbulent.

This paper focuses on the aerodynamic moment experienced by the free pitching airfoil at a specific Reynolds number, Re = 77 000. This is the Reynolds number at which a maximum amplitude of pitch oscillations has been observed by Poirel and Harris (2005) and Poirel et al. (2006, 2008). The moment is investigated using the restoring force surface method in conjunction with a least-square surface fit procedure. LES-based simulations (large eddy simulations) performed in complement to this work are then discussed and compared with the experimental results. First, some characteristics of the aeroelastic oscillations along with the experimental set-up are highlighted.

2. Aeroelastic experimental observations

The Royal Military College of Canada (RMC) wind tunnel was used for the majority of these experiments. It is a closed circuit, which can produce flow speeds ranging from 5 to 60 m/s. The wind tunnel has a test section of 0.76 m × 1.08 m and experienced a maximum turbulence intensity level less than 0.2% for the range of airspeeds considered in this work. The airspeed is measured with a pitot-static tube located at the inlet of the test section and linked to a manometer. The pitch-plunge apparatus is a two-degree-of-freedom (dof) system, composed of a rigid NACA 0012 wing moving in translation and in rotation. For both dof, two sets of pulley-spring provide the elastic restoring force. The wing span is 0.61 m and its chord is 0.156 m, thus giving an aspect ratio, AR = 3.9. End plates are installed to minimize 3-D effects. The gap between the wing tips and end plates is 7 mm, which is equivalent to 1% of the span. The wing and the end plates result in a solid blockage ratio of 5%. The axis of rotation (elastic axis, EA) of the wing can be modified; in its nominal configuration the EA is located 0.01 m forward of the quarter-chord point, i.e. at 18.6% chord aft of the leading edge. The mass ratio (based on the parts of the apparatus that rotate) is $\mu = 55.6$. The motion is measured with potentiometers and is sampled at 1000 Hz ($\Delta t = 0.001$ s). The wind tunnel and aeroelastic apparatus are schematised in Figs. 2 and 3, respectively.

The results illustrated in this paper are for the wing confined to pure rotation only; the plunge dof is held fixed. The time response reveals the loss of stability of the equilibrium point after a small perturbation, which occurs at approximately $t = 4$ s, and re-stabilization on a limit cycle oscillation (LCO). The behaviour is exemplified in Fig. 4. These oscillations are self-sustained, or limit cycle, since there is no periodicity in the upstream flow, as measured with hot-wire anemometry, accounting neither for this behaviour, nor in its wake when the wing is held fixed. Should the

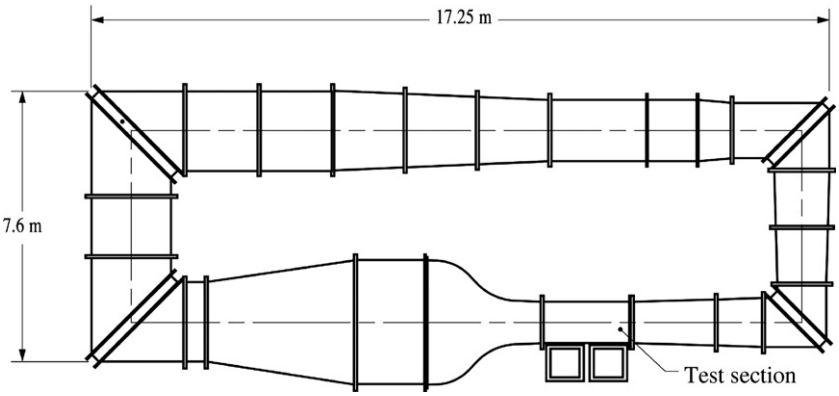

Fig. 2. The RMC low-speed wind tunnel.

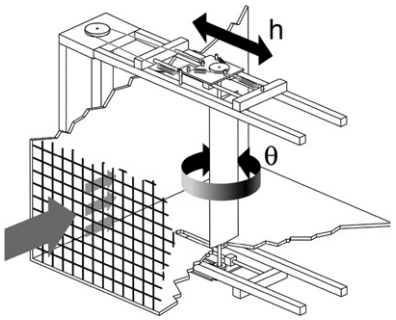

Fig. 3. Schematic of the aeroelastic apparatus.

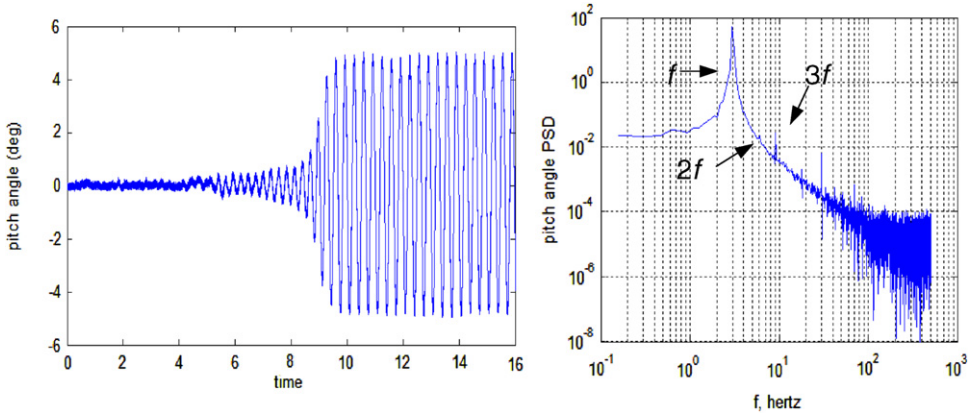

Fig. 4. Typical time response and spectral content (of LCO regime). Nominal configuration ($K_s = 0.30$, EA at $0.186c$), $U = 7.5$ m/s ($\mathrm{Re}_c = 77\,000$).

pitch motion be caused by the aerodynamics acting as an external force, a periodicity in the flow corresponding to the pitch oscillations would be expected even when the wing is rigidly fixed. This is not the case.

The oscillations exhibit essentially simple harmonic motion. The spectral content of the pitch LCO dynamics displays a single dominant frequency, f ($f = 2.9$ Hz for the case shown in Fig. 4) as well as much weaker superharmonics at 2, 3, 4 and $5f$. The even harmonics of the pitch dynamics are attributed to the small degree of misalignment that exists between the in-coming flow and the no-flow equilibrium position of the wing. No distinct dominating features are noticed at higher frequencies in the pitch response spectrum, except for the large amount of noise mainly due to the potentiometer itself and the acquisition system. Note that the peak at 30 Hz originates from the tunnel motor; its frequency does not change with airspeed. It has no noticeable influence on the LCO.

As a side note, a spectral analysis of the longitudinal (u') and normal (v') components of the wake velocity field, as measured by the hot-wire x-probe placed one chord length behind the airfoil, highlighted the presence of the pitch oscillation frequency, f, in both components, as well as harmonics at 2 and $4f$ in the u' spectrum and at $2f$ and $3f$ in the v' spectrum. Note that the dominant frequency in the u' spectrum is at twice the pitch frequency ($2f$), whereas the dominant frequency in the v' spectrum is at f. This makes physical sense from the point of view that the drag can be correlated to the longitudinal velocities attaining a positive maximum twice per oscillation cycle. On the other hand, the lift alternates between a positive and a negative maximum in one cycle, and thus correlating with the normal component. Another interesting phenomenon that was observed is a broadband peak at much higher frequencies present in both the v' and u' spectra. Expressed in terms of a Strouhal number based on the airfoil thickness, it gives $\mathrm{St} = 0.62$ ($f = 250$ Hz for the case shown in Fig. 4); details can be found in Poirel and Harris (2005) and Poirel et al. (2006, 2008). This value represents von Kármán vortex shedding, as demonstrated by Huang and Lin (1995) for a static NACA 0012 airfoil at this Reynolds number. It has no noticeable impact on the pitch LCO. In support of this conclusion, the following explanations are provided. The vortex shedding excitation is not picked up by the potentiometer (notwithstanding its limitations) and its frequency is much higher than the pitch oscillations (and wing natural frequency). Furthermore, in order to gain more insight in the phenomenon, a flow breaking grid was placed in

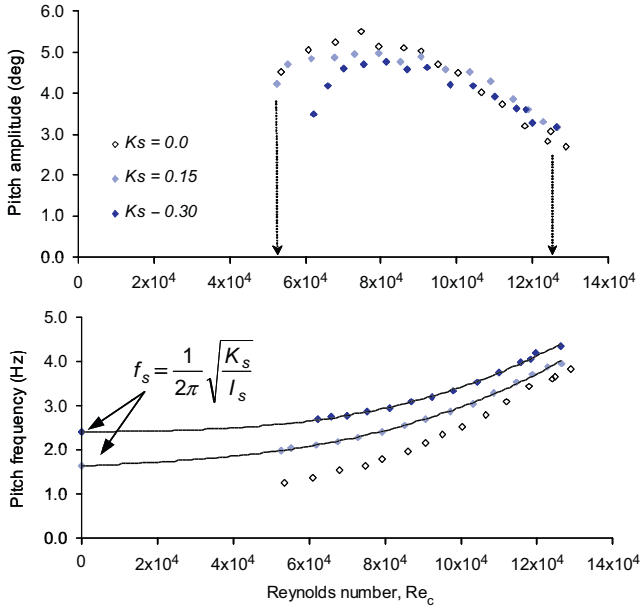

Fig. 5. Amplitude and frequency of oscillation for various stiffness coefficients. EA at 0.186*c*.

the wake of the wing and had minimal impact on the LCO, suggesting that the wake, or any coherent structures present in it, is not a factor.

In Fig. 5, the behaviour of the pitch oscillation amplitude and frequency with airspeed (Reynolds number) is plotted for various structural stiffness values. The LCO occurs for airspeeds between approximately $U = 4.5$ and 12 m/s ($5.0 \times 10^4 \leq \mathrm{Re}_c \leq 1.3 \times 10^5$). Outside of this range, they are not sustained. The maximum oscillation amplitude is observed in the case with no structural stiffness and is relatively small, below 6°. Extrapolating the oscillation frequencies toward the zero airspeed gives the structural natural frequencies, which are verified experimentally. The fact that the oscillation frequencies increase, and come together, with airspeed is attributed to the positive aerodynamic stiffness whose relative importance, in relation to the structural stiffness, also increases with airspeed.

It is worthwhile to add that the RMC's aeroelastic experiment was reproduced in a larger low-speed wind tunnel at the National Research Council of Canada (NRC). It used the same wing, pulleys and springs, but was mounted on a modified rig. The nominal free-stream turbulence intensity is comparable in both tunnels. The self-sustained oscillations were observed but within a slightly narrower range of Re, with a smaller amplitude by ~0.5–1.0° and a larger frequency by ~0.5 Hz. These differences are accounted for by the increased rotational friction that was noticed with the modified rig. The reasoning is explained in the next section.

3. Aerodynamic moment analysis

3.1. Experimental results and analysis

Considering that the flutter rig acts as a dynamic balance, the aerodynamic moment can be calculated from the recorded pitch motion. Also required are the rig structural properties. In its nominal configuration, the mass moment of inertia about the EA is $I_s = 0.00135$ kg m^2 and the structural stiffness as dictated by the springs is $K_s = 0.30$ N m. The structural damping is represented by the classical linear viscous model, $D_s = 0.002$ N m s. This assumption is justified by the no-flow pitch free decay behaviour; more details are given in Poirel et al. (2006, 2008). Hence, assuming a linear model for the rig, the aerodynamic moment is simply obtained from the following equation:

$$M_{\mathrm{EA}} = I_s\ddot{\theta} + D_s\dot{\theta} + K_s\theta. \tag{1}$$

The pitch rate and pitch acceleration are obtained by the first and second time derivatives, respectively, of the pitch time response. Because of its low (rigid-body mode) natural frequency, the high frequencies of the flexible modes which

are not accounted for, and the limitations of the potentiometer rated at 2000 rpm, the rig is not well suited to measure and investigate any high frequency content in the aerodynamics. The analysis is thus restricted to low frequencies. This focused point of view is consistent with the nature of the self-sustained aeroelastic phenomenon, which is believed to be dictated by low frequency physics. Accordingly, prior to differentiation the pitch response is first passed through a low-band-pass digital FIR filter designed in MATLAB with a sufficient high order to effectively permit a sharp cut-off. Note that the potential effect of differentiating first, and then filtering the aerodynamic moment, was examined. No perceptible differences were noted with the reverse process of filtering the pitch response first and then differentiating it, and the pitch rate, to obtain the moment.

Two cut-off frequencies are examined, one at 25 Hz which is high enough to pick up the superharmonics of any significant strength, but low enough to discard the unwanted fluctuations which could be due to measurement noise or any real physical processes not directly relevant to phenomena, such as turbulence or vortex shedding. In addition, the phase of the filter is linear. This is necessary in order to preserve the relative phase of the superharmonics for the differentiation process and subsequent combination of the pitch, pitch rate and pitch acceleration terms that form the aerodynamic moment. The other cut-off frequency, which is set at 4 Hz, serves to focus on the first or primary harmonic, thus providing the most fundamental perspective on the problem. The filter characteristics ($f_c = 25$ Hz) are shown in Fig. 6.

The differentiation is performed using a five-point scheme described in Worden and Tomlinson (2001). It is shown in Eq. (2). Once the pitch rate has been determined, the same procedure is then applied to get the pitch acceleration. A seven-point differentiation was also performed; negligible differences were noted for both the pitch rate and acceleration:

$$\dot{\theta}_i = \frac{1}{12\Delta t}(-\theta_{i+2} + 8\theta_{i+1} - 8\theta_{i-1} + \theta_{i-2}), \quad \ddot{\theta}_i = \frac{1}{12\Delta t}(-\dot{\theta}_{i+2} + 8\dot{\theta}_{i+1} - 8\dot{\theta}_{i-1} + \dot{\theta}_{i-2}). \tag{2}$$

The filtered pitch response and corresponding aerodynamic moment, normalized by $1/2\rho U^2 sc^2$, are illustrated in Fig. 7 for a time window corresponding to $6\text{ s} < t < 11.5\text{ s}$ in Fig. 4. Their respective spectral representation of the LCO regime (using the last 18 pitch oscillation cycles which is the time window corresponding to $10\text{ s} < t < 16\text{ s}$ in Fig. 4) is shown in Fig. 8.

Even though the pitch response is very clean, the aerodynamic moment is not well behaved. The super-harmonics are amplified by the differentiation process. An important physical distinction can be made between the even and odd harmonics. As stated earlier, the former are due to the slight misalignment between the flow and the airfoil. In theory, given perfect alignment they should not appear. Later in the paper, this point will be further discussed. For the odd harmonics, the $3f$ component is the dominant one and is significant in comparison with the fundamental frequency. The presence of harmonics, namely the odd, is a strong indication of the nonlinear nature of the aerodynamic moment.

A different and instructive perspective is obtained by plotting the aerodynamic moment coefficient as a function of pitch angle. This is shown in Fig. 9 for the two cut-off frequencies. The left-hand plot is for the higher cut-off frequency at 25 Hz. The cut-off frequency at 25 Hz, for which the important contribution of the super-harmonics is clearly visible, does not permit any visual interpretation. Accordingly, the right hand plot, for the cut-off frequency ($f_c = 4$ Hz) just above the fundamental frequency ($f = 2.9$ Hz) of the LCO, serves the purpose to more easily explain the dynamics at play. The growing small amplitude loops, at the centre of the plot, correspond to the first few seconds of oscillations, as shown in Fig. 7, whereas the larger loops represent the steady state LCO. The clockwise direction of the loops, as indicated by the arrow,

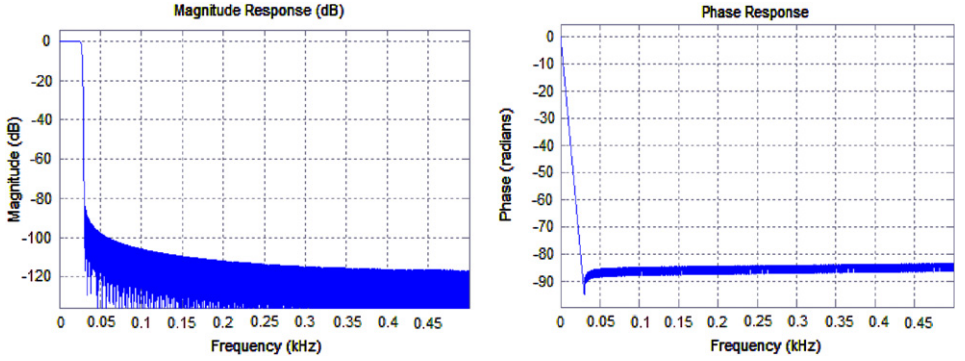

Fig. 6. Magnitude and phase response of digital FIR filter, $f_c = 25$ Hz.

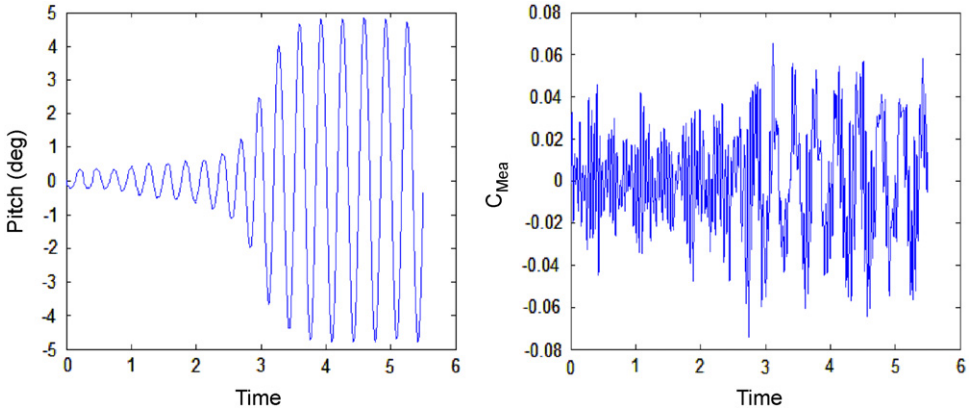

Fig. 7. Filtered pitch response ($f_c = 25$ Hz) and aerodynamic moment coefficient as a function of time. Nominal configuration ($K_s = 0.30$, EA at $0.186c$), $U = 7.5$ m/s ($\mathrm{Re}_c = 77\,000$).

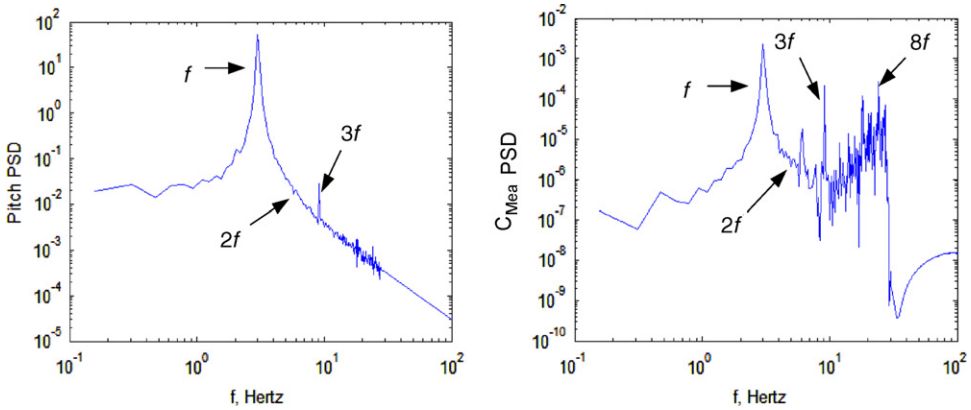

Fig. 8. Filtered pitch response PSD ($f_c = 25$ Hz) and aerodynamic moment coefficient PSD for LCO regime. Nominal configuration ($K_s = 0.30$, EA at $0.186c$), $U = 7.5$ m/s ($\mathrm{Re}_c = 77\,000$).

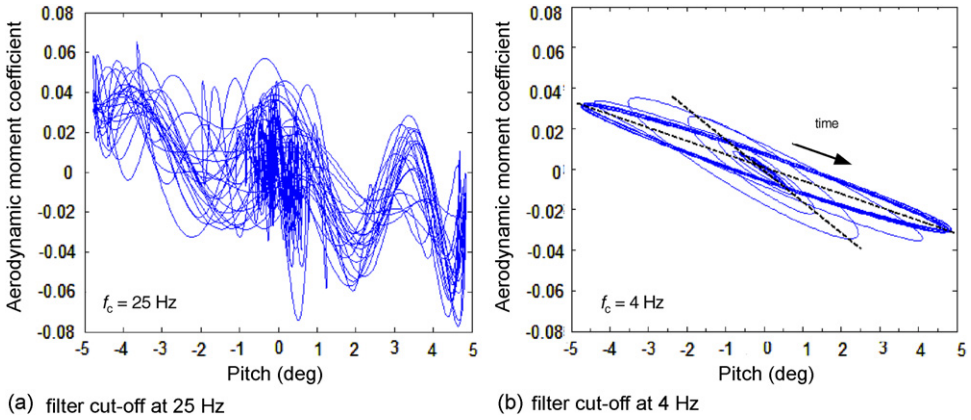

Fig. 9. Aerodynamic moment coefficient as a function of pitch angle during the transitory and LCO regimes, for two different filter cut-off frequencies. Nominal configuration ($K_s = 0.30$, EA at $0.186c$), $U = 7.5$ m/s ($\mathrm{Re}_c = 77\,000$).

physically means that the work done by the airflow on the airfoil is positive. In other words, the aerodynamic damping is negative and the flow transfers energy to the structure and sustains the oscillations. Hence, they are self-sustained from an aeroelastic point of view. The work per cycle, averaged over 18 LCO cycles, is calculated to be $W_{\mathrm{aero}} = 0.0009$ N m.

The rotation of the main axis of the elliptical shape, shown with the dashed lines, provides some indications about the change of the aerodynamic stiffness as the oscillation amplitude grows with time until the dynamics reach the steady-state LCO. The larger slope of the axis at small pitch amplitudes compared with the smaller slope at larger pitch amplitudes means that the aerodynamic stiffness decreases with pitch angle. The change of stiffness with pitch amplitude can be physically related to the movement of the LSB, purely on the basis of static considerations. Taking into account that the LSB is a localized region where the flow is separated, it is associated with a pressure plateau at a lower value should it had remained attached. Past the re-attachment point, the pressure rises again. Furthermore, close to the leading edge the suction peak decreases to a larger pressure value due to the (local) separation as similarly demonstrated by Lutz et al. (2001). Assuming that the elastic axis is located between the suction peak and the LSB, the combination of the relative high pressure ahead of the EA and low pressure aft of the EA, respectively, causes a pitch down stabilizing moment, similar to high AOA stall. As the pitch angle is increased, the bubble moves forward (assuming a static airfoil) thus reducing its impact on the moment since its lever arm becomes smaller, ultimately decreasing the aerodynamic torsional stiffness.

In Fig. 10, the time history of the aerodynamic moment coefficient is superimposed over the pitch displacement for the 4 Hz cut-off case. Consistent with the previous discussion, as the amplitude grows the period of oscillation also increases. Indeed, the frequency of the transient oscillations, where the amplitude is small, is higher (3.6 Hz at $t = 2$ s) than the steady-state LCO frequency (2.9 Hz). Also observed is the moment lagging the pitch displacement, which is consistent with positive work done by the flow and negative aerodynamic damping. The lag is best seen at the zero axis where there is slight delay of the moment compared with the pitch motion.

Empirical aerodynamic moment modelling: The application of the restoring force surface method, in conjunction with a surface fitting procedure, provides a more rational framework to capture the aerodynamic moment characteristics. This system identification method has been applied with success to different problems and is particularly attractive for a single-degree-of-freedom system due to its simplicity. Details are provided in Worden and Tomlinson (2001). Applied to the current problem, the idea is as follows. Starting with Eq. (1), and using Eq. (2), the aerodynamic moment is calculated for a given time period. It is then plotted as a function of the pitch displacement and pitch rate. This plot, exemplified in Fig. 11 for the nominal case and $f_c = 25$ Hz, is assumed to contain all the relevant information about the aerodynamic moment for the problem under investigation. Note that the view facing the C_{Mea}—θ plane, or parallel to the pitch rate axis, is the same as the left-hand plot of Fig. 9.

Implicit to this formulation is the assumption that the aerodynamic moment is not an explicit function of the pitch acceleration and the time, which in effect is a quasi-steady approximation:

$$M_{\mathrm{EA}}(\theta, \dot{\theta}, \ddot{\theta}, t) \approx M_{\mathrm{EA}}(\theta, \dot{\theta}). \tag{3}$$

The pitch acceleration term represents the effect of added mass of the fluid. It can be neglected on the basis of a large mass ratio, $\mu = 55.6$, and a combination of a low pitch frequency and small amplitude. The time dependency reflects the effect of the shed vorticity in the wake caused by the pitching motion on the airfoil itself. Although its impact is felt upstream on the airfoil, each element of vorticity sees its effect diminishing in time as it is convected downstream with speed, U. Accordingly, the larger the airspeed U, the less effect it has. Inversely, the larger the pitching frequency, the greater effect it has. This can be expressed by the reduced frequency, $k = \omega c/2U$. For linear aerodynamics, which is not the case here, the unsteady effects due to the shed vorticity can generally be neglected for $k < 0.05$. In this work, the pitch oscillation frequencies, in reduced form are in the order of 0.1–0.2. They are slightly higher than 0.05 but still of

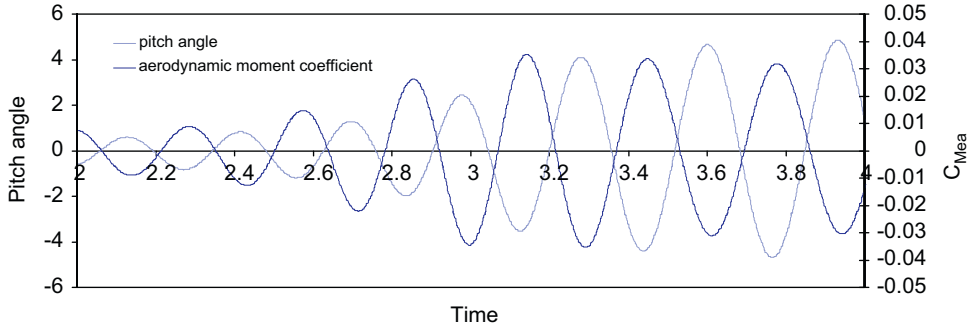

Fig. 10. Filtered pitch response ($f_c = 4$ Hz) and aerodynamic moment coefficient as a function of time. Nominal configuration ($K_s = 0.30$, EA at $0.186c$), $U = 7.5$ m/s ($\mathrm{Re}_c = 77\,000$).

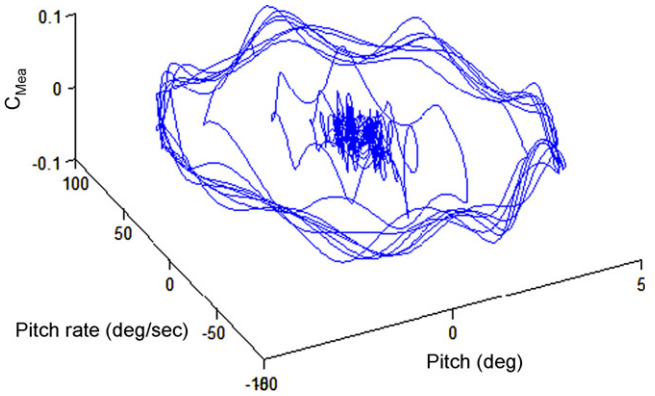

Fig. 11. Aerodynamic moment coefficient as a function of pitch angle and pitch rate. Nominal configuration ($K_s = 0.30$, EA at 0.186c), $U = 7.5$ m/s ($\mathrm{Re}_c = 77\,000$), $f_c = 25$ Hz.

the same order of magnitude. It is assumed that this linear aerodynamic limit can be applied, more or less, to the nonlinear case. Along this note, it is worthwhile to repeat that the experimentally observed pitch oscillations were not affected significantly by the presence of objects placed in the airfoil's wake. These considerations justify, to some extent, the quasi-steady approach.

A least-squares surface fitting procedure is then applied to the experimental data. In this work a third order polynomial is used in both states. It is in some sense a generalized Duffing–van-der-Pol type nonlinear model. It is given by

$$C_{M_{\mathrm{EA}}}(\theta,\dot{\theta}) = a_1 + a_2\theta + a_3\dot{\theta} + a_4\theta^2 + a_5\theta\dot{\theta} + a_6\dot{\theta}^2 + a_7\theta^3 + a_8\theta^2\dot{\theta} + a_9\theta\dot{\theta}^2 + a_{10}\dot{\theta}^3. \tag{4}$$

Based on the physics of the problem, whereby the airfoil oscillates about the zero angle of attack and the expected symmetry of the aerodynamic moment about the pitch angle and pitch rate, all even terms in the model are constrained to be zero ($a_1 = a_4 = a_5 = a_6 = 0.0$). Accordingly, the terms left are linear and cubic. This is consistent with our observations of the dynamics since the cubic super-harmonic is the dominant one for both the experimental, and LES results as will be discussed later.

There are basically two parts to the model. The Duffing part (θ, θ^3) represents the static (or stiffness) contribution to the aerodynamic moment. Published static aerodynamic moment data in this range of transitional Re numbers for similar wings display a nonlinear moment–AOA relationship very much compatible with the Duffing model at small angles of attack; see Fig. 1 for instance. The van-der-Pol part ($\dot{\theta}$, θ^2, $\dot{\theta}$) accounts for the dynamic (or damping) modelling. It is often used to describe qualitatively the phenomenon of stall flutter. We choose a more general form that includes the additional terms ($\dot{\theta}^2$, θ, $\dot{\theta}^3$), hence the name generalized Duffing–van-der-Pol model.

The robustness of the model was evaluated on a number of fronts. First, it consisted in investigating the sensitivity of the odd term parameters to the presence of the even term parameters. It was found that the values of the odd parameters were very robust and changed very little when the constraint of nullifying the even parameters was removed. A completely different approach to the least-square fit was also used to estimate the parameters, which consisted in applying a hybrid Ensemble Kalman-Particle Filtering technique (EnK-PF); see Khalil et al. (2009) for details. It showed a very good match between the two sets of model parameters obtained from very distinct techniques. In addition, the EnK-PF technique was also applied to evaluate a 5th order model. It was observed that the 5th order terms had minimal influence on the linear and 3rd order parameters; the latter were thus considered to be robust.

The actual model, at this particular Reynolds number, is given by Eq. (5), where the pitch angle is expressed in radians:

$$C_{M_{\mathrm{EA}}}(\theta,\dot{\theta}) = -7.76\times10^{-1}\theta + 1.35\times10^{-2}\dot{\theta} + 5.04\times10^{1}\theta^3 - 3.10\theta^2\dot{\theta} + 2.20\times10^{-1}\theta\dot{\theta}^2 - 2.39\times10^{-3}\dot{\theta}^3. \tag{5}$$

It is plotted in Fig. 12. Note that only the moment's values that correspond to the range of experimentally observed combinations of pitch angle-pitch rate are physically relevant. Hence, looking down the moment coefficient axis on the pitch angle-pitch rate plane, the region covered is an image of the system state trajectories in the phase plane. Outside this range, the fit provides an extrapolation of the aerodynamic moment coefficient and is therefore not valid.

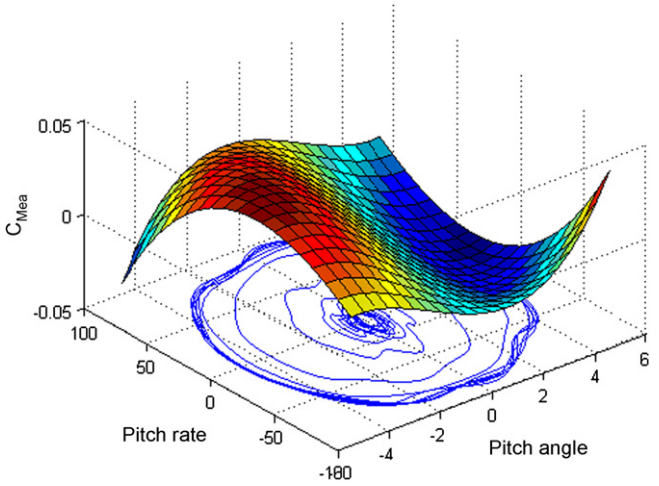

Fig. 12. Third order surface fit of aerodynamic moment coefficient as a function of pitch angle and pitch rate. Nominal configuration ($K_s = 0.30$, EA at 0.186c), $U = 7.5$ m/s ($\mathrm{Re}_c = 77\,000$), $f_c = 25$ Hz.

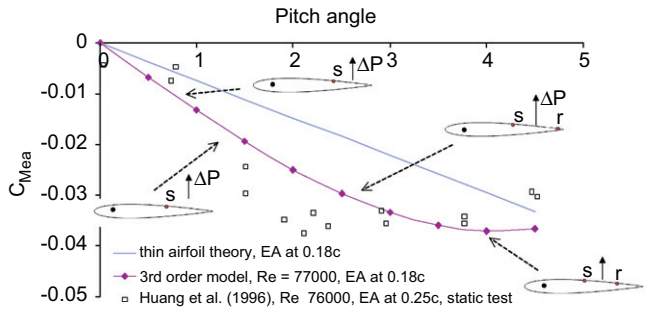

Fig. 13. Aerodynamic moment coefficient versus pitch angle for zero pitch rate and schematic of separation region and related moment–force on suction side.

In comparison with Fig. 11 the fitting procedure has obviously a smoothing effect on the moment. In effect, the fitting eliminates the high frequency content of the aerodynamic moment. This will be exemplified in the next section. It enables a more focused perspective on the low frequency aerodynamics and is compatible with the quasi-steady model. For the range of pitch angle and pitch rate studied in this work, the aerodynamic moment is highly nonlinear in both angle and rate. This nonlinear behaviour, even for small angles ($\theta \leq 5^\circ$), is not surprising. It is a direct consequence of the complex flow physics occurring at transitional Reynolds numbers.

Looking at the moment-angle plane for a zero pitch rate, the static case $C_{\mathrm{Mea}}(\theta)$ emerges and is reproduced in Fig. 13 for positive pitch angles. Also plotted for comparison is the linear thin airfoil theory model, as well as the experimental results from Huang et al. (1996), which were shown in Fig. 1. The agreement between Huang's and the current work's results is good but not exact. This is expected due to some differences in the two configurations. Both are for a NACA 0012 type airfoil at $\mathrm{Re}_c \approx 77\,000$ and $\mathrm{Tu} \approx 0.2\%$. The differences are in the axis about which the moment is calculated, 0.186c for the current work and 0.25c for Huang et al. (1996), and in the wing configuration, free rotating wing with plates at both ends for the current work (i.e. quasi-2-D case) and a cantilevered wing with one end plate for Huang et al. (1996) (i.e. stronger 3-D effects at wing tip). A subtle difference exists at the very small angles. It was believed to be related to the order of the nonlinearity considered for the least-square fit; however, higher-order polynomial models did not capture the change in slope at these angles. It may well be due to experimental uncertainties and non-uniformity of the flow in Huang et al. (1996), since one would expect a zero moment at zero angle of attack.

Also illustrated in Fig. 13 is a schematic of the separation region and related moment–force on the suction side, as inferred from Huang et al. (1996) for the NACA 0012 and more general works (Gad-el-Hak, 1990; Mueller, 1985; Lutz et al., 2001) on low-Re flows. ΔP describes the suction force due to the LSB or the open separation. Its relative magnitude is represented by the length of the vector, which is assumed to be proportional to the length of the LSB or

the open separation. This vector force is applied at the middle of the LSB. Also shown is the axis of reference for the moment, located at $0.18c$. As the angle of attack is increased from 0° the separation point moves forward which in turn enlarges the region of flow separation, cumulating in a growing pitch down moment. The behaviour of the moment with angle of attack, from 0° to 2–3°, is representative of laminar trailing-edge separation without re-attachment. At about $\alpha \approx 3^\circ$, trailing-edge re-attachment occurs. For further increases in angle of attack, both the separation point and re-attachment point move forward, the latter advancing slightly faster, thus resulting in a LSB with a decreasing length. The smaller LSB coupled with a decreasing moment arm cause for the leveling of the moment at $\alpha \approx 3$–5°.

Taking a slice in Fig. 12 at a given pitch angle on the aerodynamic moment coefficient—pitch rate plane is relevant to analyse the aerodynamic damping. Although no direct experimental results have been found in the public literature to validate the pitch rate contribution, the aerodynamic moment coefficient as a function of pitch rate, taken at zero pitch angle, makes sense physically. It is shown in Fig. 14.

The slope at zero pitch rate is positive which implies negative aerodynamic damping at these conditions. This is given by the coefficient a_3 in Eq. (4); $a_3 = 0.01354\ (\mathrm{rad/s})^{-1}$ as per Eq. (5). Note that a positive a_3 translates into a negative aerodynamic damping coefficient when it is moved on the other side of Eq. (1) and combined with the structural terms as shown below:

$$I_s\ddot{\theta} + \left[D_s - 1/2\rho U^2 sc^2(a_3 + a_8\theta^2 + a_{10}\dot{\theta}^2)\right]\dot{\theta} + \left[K_s - 1/2\rho U^2 sc^2(a_2 + a_7\theta^2 + a_9\dot{\theta}^2)\right]\theta = 0. \tag{6}$$

By making (a_3) dimensional, via its multiplication by $1/2\rho U^2 sc^2$, it can be compared directly with the structural damping coefficient, D_s. The value of the dimensional a_3 is 0.0068 N m/(rad/s). Its magnitude is larger than the structural damping coefficient, $D_s = 0.002$ N m/(rad/s), thus resulting in the loss of stability of the equilibrium point with a fluttering behaviour. It is important to realize that the negative aerodynamic damping cannot be attributed to the single-degree-of-freedom (sdof) type flutter, reported by Runyan (1951) or Bisplinghoff et al. (1983) for instance. Although unsteady linear (inviscid) aerodynamic can predict sdof pitch instability, it does occur only for very large values of the so-called inertia parameter, $\overline{I} = I_s/(s\rho\pi b^4)$. For the specific values of parameter investigated in this work, in particular for the small inertia $\overline{I} = 16$, and using a two-state representation of Wagner's lift-deficiency function (see Bisplinghoff et al., 1983 for instance) no such flutter is predicted. This is so even when accounting for the airfoil's thickness by modifying Wagner's parameters based on Cebeci et al. (2005)'s panel method calculations. The mass moment of inertia would have to be increased two orders of magnitude for (inviscid) sdof flutter to be possible.

As the oscillations grow and stabilize onto an LCO, the higher-order damping terms in Eq. (4), namely a_8 and a_{10}, become dominant. These terms are negative; hence provide positive aerodynamic damping, which counteracts the dynamically de-stabilizing effect of the a_3 coefficient.

The primary reasons for developing such a model are to serve as a (experimental) data reduction tool providing a relevant comparison basis with existing static results, and to help validate the low-frequency content of the LES results. For the static results comparison, Fig. 13 is providing some validation and subsequent discussion. For the LES results, by means of comparing the experimental/model aerodynamic moment with the numerical aerodynamic moment, the validated LES can then be used to obtain insights into the flow physics associated with the pitch oscillations at these transitional Re. Specifically, the model is useful to bypass the problems associated with the phase-averaging of the experimental aerodynamic moment since there are cycle-to-cycle variations in the period length.

It is worthwhile to add that the model demonstrated some ability to predict dynamical behaviour in different conditions from those used to develop it, namely at conditions other than $\mathrm{Re}_c = 77\,000$. The empirical model developed

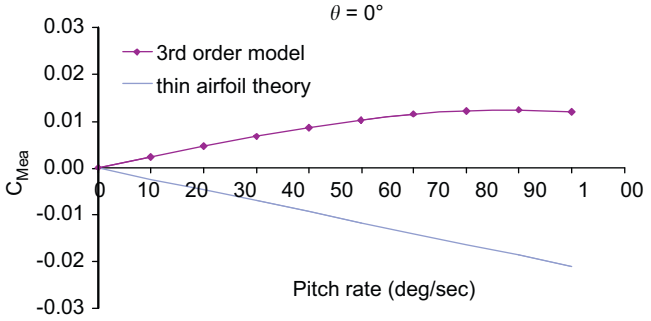

Fig. 14. Aerodynamic moment coefficient versus pitch rate for zero pitch angle.

for $Re_c = 77\,000$ was used as an input into an aeroelastic numerical model of the experimental set-up and tested for the same range of Reynolds number shown in Fig. 5. As a qualitative result, the model predicts reasonably well the overall pitch oscillation amplitude and frequency behaviour as a function of Re, for instance the increase followed by a decrease of the amplitude with Reynolds number.

3.2. Computational fluid dynamic (CFD) analysis

In order to gain additional in-sight into the physical mechanisms at play during the self-sustained pitch oscillations, numerical simulations were performed using the NRC-IAR in-house code INSFlow (Yuan and Khalid, 2004) which has been used for a number of LES and URANS (unsteady Reynolds-averaged Navier–Stokes) calculations for various flows in incompressible regimes, i.e. Yuan et al. (2006, 2007a). The LES-based method was chosen for this study as the LES concept had shown a capability of simulating transitional separated flows (Yuan et al., 2006, 2007a). It is important to note that these simulations are purely fluidic, not aeroelastic; there is no coupling with the structural model. The pitch motion schedule measured in the experiments was taken as an input for the calculations.

2-D calculations of flows past both stationary and pitching NACA 0012 airfoil were initially carried out for a range of Reynolds numbers within and outside the LCO region (Yuan et al., 2007b). These parametric studies were performed in 2-D owing to the high CPU time cost caused by 3-D calculations. In this work, 3-D simulations are performed and reported for the nominal case, $Re_c = 77\,000$. A simple harmonic motion (SHM) pitch input, $\theta = 5.1\sin(2\pi ft)$ with $f = 2.9$ Hz, is used since the superharmonics in the pitch aeroelastic response are very weak; refer to Fig. 4. The 2-D solution (Yuan et al., 2007b) is used as a start solution for the 3-D calculations. Eleven cycles of pitch oscillations are carried out. The last ten cycles, which corresponds roughly to 161 flow-through-time units (c/U), are then used for the analysis. The far field is set at 10 chords away from the airfoil. The span is assumed to be 6.4% chord for the 3-D calculations and a periodic boundary condition is used in the spanwise direction.

Based on their direct numerical simulations (DNS) of riblet flows, Choi et al. (1993) recommended a non-dimensional Courant–Friedrichs–Lewy (CFL) number of unity for deciding the time step in turbulent simulations; $CFL = \Delta t/\max(|\Delta x/u|, |\Delta y/v|, |\Delta z/w|)$. The time step used in the current computations is $\Delta t = T/3840 = 8.98 \times 10^{-5}$ s, where T is the period of one pitching cycle, i.e. $T = 1/2.9$ s for the nominal case. This time step results in a non-dimensional CFL number of about 1 at the static condition. As the pitching motion increases flow velocity in some regions, the resulting local CFL number is increased to 1.5–3 in some regions in the dynamic test case, which actually indicates potential for further refinement of the solution at some extra computational cost in the near future.

The design of an adequate mesh is always an important issue in large-eddy simulations, which involves several aspects. The most energetic eddies of the boundary layer have to be resolved. The criteria of the grid resolution depend on the numerical method employed (Lund et al., 1995). The mesh resolution with spacing $\Delta x^+ = 100$ and $\Delta z^+ = 20$ in wall unit is usually required by LES of wall-bounded flows (Mary and Sagaut, 2002). In this work, an O–H type grid ($481 \times 65 \times 17$) is generated based on the understanding and experiences gained from previous research work (Yuan et al., 2006, 2007a; Mary and Sagaut, 2002). Fig. 15 shows evolution of the mesh resolution in the boundary layers in wall units at two representative time instants based on the 10-cycle phase-averaged flow field of the 3-D unsteady calculations, which confirms that the aforesaid requirement is satisfied in almost all the flow field in the boundary layer

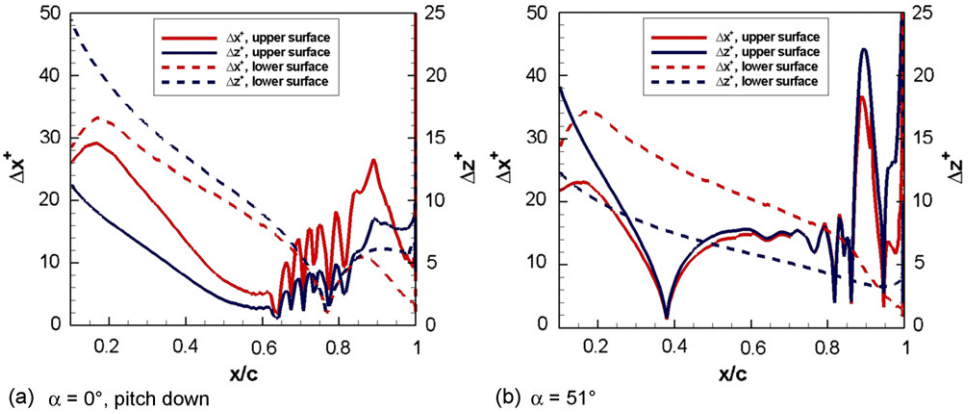

Fig. 15. Evolution of the grid resolution in wall unit in the boundary layer of the NACA 0012 rectangular wing based on spanwise and phased-averaged 3-D LES results at $Re_c = 77\,000$ and $\alpha = 5.1^\circ \sin(2\pi ft)$ with $f = 2.9$ Hz.

with a mesh size reaching $\Delta x^+ \leq 50$ and $\Delta z^+ \leq 20$. The wall-resolved simulations of channel flows in Davidson et al. (2003) suggested the requirement to capture the near-wall layer down to $y^+ \sim 2$, with grid density increasing toward the wall at a rate not bigger than 10%. This recommendation was considered in the grid generation but with a slightly larger extension rate. As a result, the maximum value of y^+ for the first grid point at the wall is 0.4 in the calculations, with at least 21 grid points inside the boundary layer over most of the surface. The inner part of the O-type mesh pitches rigidly, in unison with the airfoil, while the outer part remains stationary. The mesh layer between the inner and outer parts is dynamic, rather than sliding, and deforms during the airfoil pitching motion. This is doable as the deformations are small. Furthermore, in order to accelerate the calculations, the computation domain is divided into five blocks for parallelization.

The spanwise extent of the computational domain places an upper limit on the size of the flow structures that may be represented. If this is chosen too small, it becomes difficult to ensure the physical realism of the computed flow. The European LESFOIL project has investigated its effect on the LES results (Mellen et al., 2003). The test cast was an Aerospatiale A-airfoil at $Re_c = 2.1 \times 10^6$ and $\alpha = 13.3^\circ$. Both laminar flow separation at leading edge and turbulent flow separation at trailing edge were observed in the experiments. Based on the estimated size of the likely flow structures in the trailing-edge separation, it was initially suggested that an acceptable minimum would be $0.12c$. This corresponds to about 1.5δ at the trailing edge. However, except for one of the seven partners, a smaller span than this value was used as this required much higher computational resources to match the reasonable spanwise resolution Δz^+. Because an adequate spanwise resolution is one of the key requirements for the success of an LES as discussed below, most partners reduced the span extent, at the risk of altering to some extent the largest-scale features of the flow. The results showed that this turned out to be a successful compromise. Mary and Sagaut (2002) used $0.012c$ as the span length for this test case and performed the well-known first successful airfoil LES in aeronautical applications. They successfully predicted both the leading-edge and trailing-edge separations. The reduction in spanwise extent influenced adversely the computed flow only in the trailing-edge region (Mellen et al., 2003). Using a $0.06c$ as the spanwise extent, Mellen et al. predicted fairly realistic $v'v'$ and $u'v'$ fluctuations, in particular in the near wall region. For another NACA 0012 test case at $Re_c = 1 \times 10^5$ and $\alpha = 4^\circ$, Shan et al. (2005) used $0.1c$ as span length in their direct numerical simulation (DNS).

In the current study, as a compromise between the real physics and computational cost, the span was assumed to be $0.064c$ for the 3-D calculations with a periodic boundary condition in the spanwise direction. To assess the adequacy of the current span extent for capturing the major features of the flow, the two-point velocity correlation function is used as reference. Fig. 16 shows the correlations of the streamwise velocity along the span at $\alpha = 0^\circ$. According to the previous 2-D simulations (Yuan et al., 2007b) and confirmed by the current 3-D simulations, $\alpha = 0^\circ$ is the critical point for the clockwise running of the pitching moment, which maintains the positive work done by the fluid to the airfoil as discussed later. The x-locations were selected to represent the laminar separation, transition, reattachment and other two points near the trailing edge. As shown in the figure, a correlation value of ~ 0.2 is reached at the mid-span region.

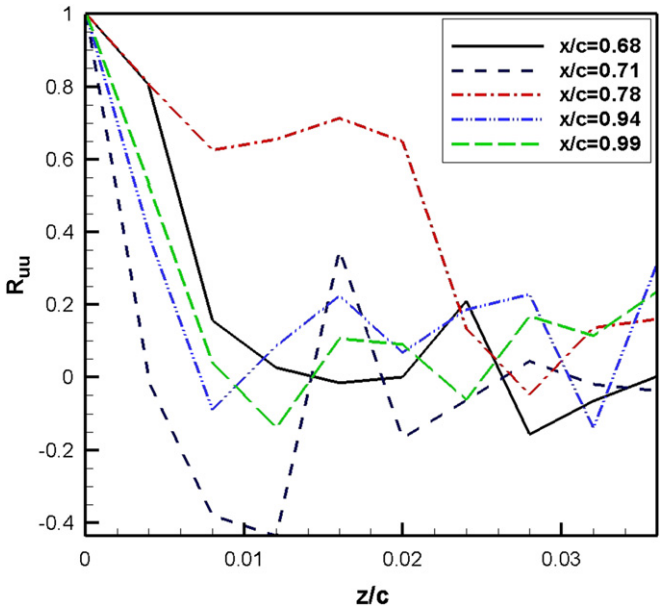

Fig. 16. Two-point velocity correlations based on the streamwise velocity obtained by LES for $\alpha = 0^\circ$ top surface when pitch down.

The actual 3-D flow structure is presented in Fig. 17 which shows iso-surfaces of spanwise, streamwise, and cross-stream-direction vorticities over the top surface of the wing at two different time instants (corresponding to phases c and f discussed later). The spanwise vorticity in the top plot clearly shows 2-D shear layer and its distortion to 3-D structure near the trailing edge. In addition, the streamwise and cross-stream-direction vorticities confirms nonuniform flow structure along the wing span implying probable inaccuracy of 2-D assumptions used in the 2-D calculations. Additional details can be found in Yuan et al. (2008).

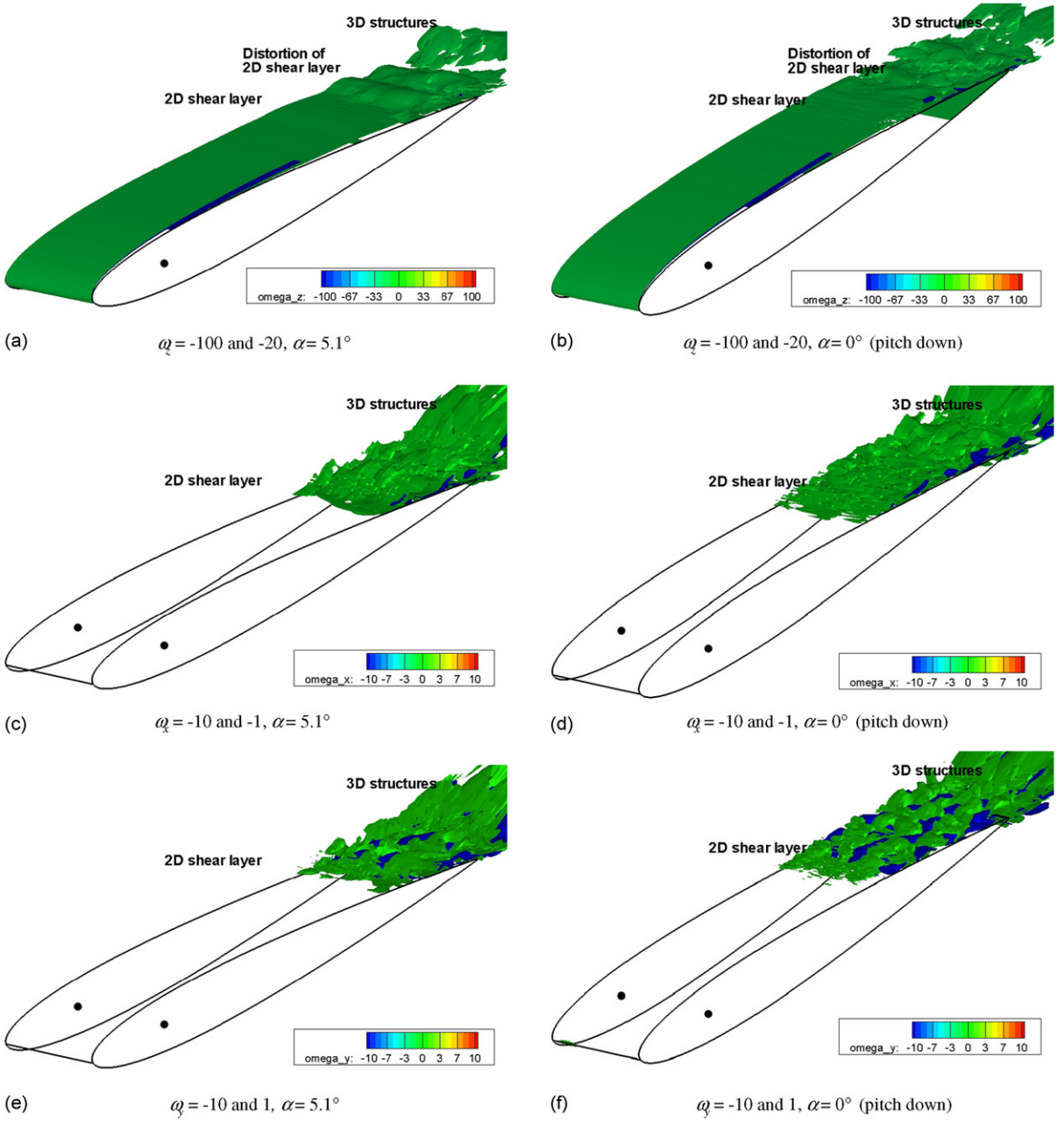

Fig. 17. Iso-surfaces of nondimensional instantaneous spanwise (top), streamwise (middle), and crossstream-direction (bottom) vorticities over the NACA 0012 rectangular planform wing at $Re_c = 77\,000$ and $\alpha = 5.1^\circ \sin(2\pi ft)$ with $f = 2.9$ Hz. Left: $2\pi ft = \pi/2$; right: $2\pi ft = \pi$.

Figs. 18 and 19 show the lift and aerodynamic moment time histories, respectively. In addition, their spectral content is displayed in Fig. 20, in the left and right plots, respectively. The lift is well behaved and almost purely simple harmonic, suggesting that its behaviour is nearly linearly dependant on the pitch angle at these small amplitudes. The 3*f* superharmonic is two orders of magnitude smaller than the fundamental frequency. On the other hand and similar to the experimental results, there is significant superharmonic activity for the moment, the main being at 3*f*, even though the input is purely harmonic for the simulations. Of note is the fact that no even harmonics are present since the airfoil is perfectly aligned in the calculations. The root-mean-square value of the filtered ($f_c = 25$ Hz) LES and experimental aerodynamic moment coefficients are 0.023 and 0.028, respectively, which are comparable. The differences might be attributed to the aeroelastic coupling in the experimental case, which may increase the aerodynamic moment magnitude

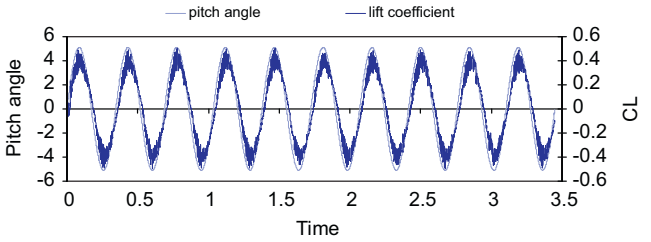

Fig. 18. Prescribed pitch motion, $\theta = 5.1^\circ \sin(2\pi ft)$ with $f = 2.9$ Hz, and lift coefficient as a function of time. LES calculations at $\mathrm{Re}_c = 77\,000$.

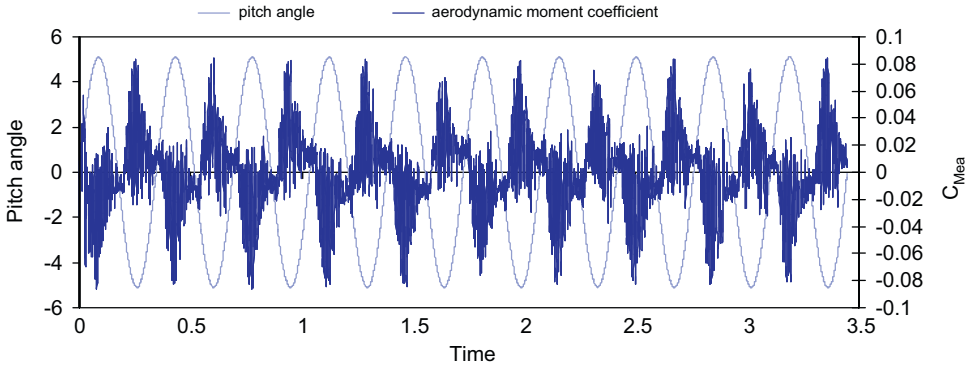

Fig. 19. Prescribed pitch motion, $\theta = 5.1^\circ \sin(2\pi ft)$ with $f = 2.9$ Hz, and aerodynamic moment coefficient (EA at 0.186*c*), as a function of time. LES calculations at $\mathrm{Re}_c = 77\,000$.

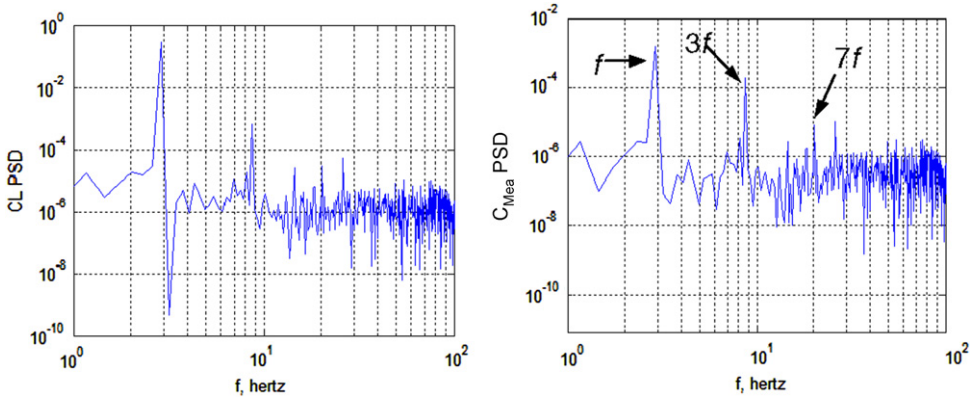

Fig. 20. Lift coefficient PSD and aerodynamic moment coefficient (EA at 0.186*c*) PSD for LCO regime. LES calculations for $\theta = 5.1^\circ \sin(2\pi ft)$ with $f = 2.9$ Hz, $\mathrm{Re}_c = 77\,000$.

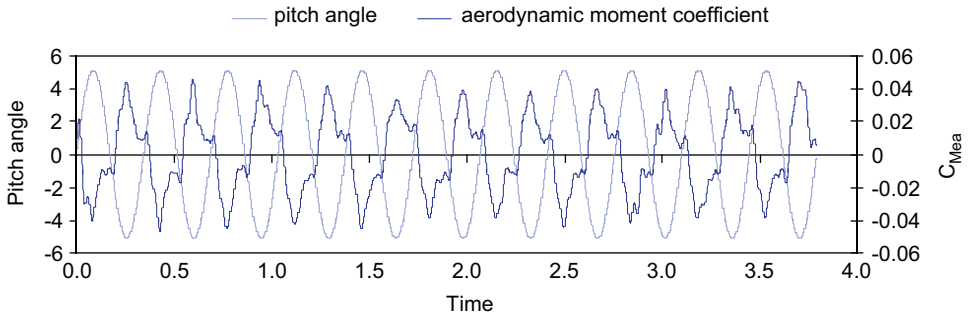

Fig. 21. Prescribed pitch motion, $\theta = 5.1^\circ \sin(2\pi ft)$ with $f = 2.9$ Hz, and filtered ($f_c = 25$ Hz) aerodynamic moment coefficient (EA at $0.186c$) as a function of time. LES calculations at $\mathrm{Re}_c = 77\,000$.

via a feedback mechanism with the pitch motion and by the airfoil-flow misalignment, which is manifested as even harmonics in the moment PSD for the experimental case.

To enable a more rational comparison with the experimental results, and using the same logic of focusing on the low frequency content of the problem, the LES-based moment calculated about the axis of rotation at $0.18c$ is low-pass filtered, as shown in Fig. 21 for $f_c = 25$ Hz. At the zero crossing, the moment is lagging the pitch motion, which is consistent with the experimental results. Indeed, the work done by the flow is calculated to be $W_{\mathrm{aero}} = 0.0011$ N m, nearly the same as for the experiment. This is an essential finding as it confirms that the simulations are able to predict, albeit indirectly (since there is no aeroelastic coupling), the self-sustained nature of the pitch oscillations.

The empirical aerodynamic model developed in the previous section can now be evaluated against the LES calculations with confidence. A SHM time history, of pitch and pitch rate, is fed into Eq. (5) for one complete cycle of oscillation. The results are shown in Fig. 22, superimposed on the 25 Hz-filtered span- and phase-averaged LES solution. The comparison is very good, especially considering that the 3rd order empirical model can only reproduce the fundamental and the 3rd superharmonic. Moreover, it justifies to some degree the implicit quasi-steady formulation of the model for this problem. The moment is lagging the pitch motion at the very small angles around the origin, as shown for phase *f*, or at 180°, on the figure. At phase *c*, or 90°, the moment leads slightly the motion.

In the same vein, the moment-pitch angle representation is analysed in Fig. 23. The arrows indicate the direction with time. The comparison is also very good. The change of direction of the loop at both ends of the ellipse, indicative of negative work in these two small regions, is handled reasonably well by the empirical model.[1] The work done by the flow calculated over the complete cycle for the empirical model is $W_{\mathrm{aero}} = 0.0007$ N m, and is comparable with the LES case. Finally, the slope of the main axis of both ellipses is about the same, indicating that the aerodynamic stiffness is also captured correctly by the empirical model. Also displayed in Fig. 23 are two sets of unsteady linear (inviscid) aerodynamics theory results, based on Theordorsen's (or Wagner's) function and then modified to account for the airfoil thickness (as per Cebeci et al. (2005)). The main differences between the linear and nonlinear results are the well defined elliptical shape for the linear case, and most importantly the counter-clockwise direction indicating negative work done by the flow (or positive aerodynamic damping) also for the linear model. In other words, unsteady linear aerodynamics does not predict the self-sustained oscillations as stated in Section 3.1.

The next figure illustrates some details of the flow field for the six representative phases of the cycle (a–f) indicated in Figs. 22 and 23. The pressure coefficient, skin-friction coefficient and Reynolds shear stress shown have been span- and phase-averaged. In this analysis, we loosely use the conventional static definition of boundary layer separation where the wall shear stress vanishes, in conjunction with a flattening of the pressure coefficient post a region of adverse pressure gradient. This is exemplified for phase d ($\alpha = 3.1^\circ$ pitch down), where both upper surface and lower surface separation is observed. The identification of the re-attachment point is more ambiguous due to the strong unsteadiness of the flow in this region; even though the figure shows span- and phase-averaged values recall that only 10 pitch oscillation cycles were performed. However, the non-monotonic behaviour of the friction coefficient in the LSB cannot solely be attributed to a restricted number of cycles, hence phase averages. It has also been observed for static cases

[1]Interestingly, the same topology with a larger inner loop and two smaller lobes, characterizing the aerodynamic moment—angle of attack relationship, has been observed in transonic inviscid flow dynamic simulations for small angles (Voß and Wegner, 1992). In this case, the source of the nonlinearity is the movement of the shock wave, as opposed to boundary layer separation and/or LSB. This similarity in dynamics between these two canonical flow regimes, transonic and transitional flows, is worth exploring.

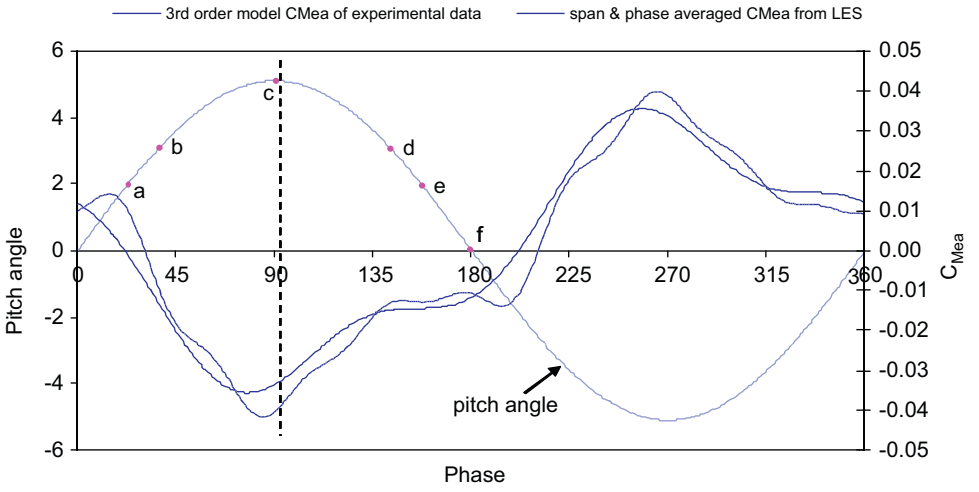

Fig. 22. Pitch angle [$\theta = 5.1^\circ \sin(2\pi 2.9t)$], span- and phase-averaged filtered ($f_c = 25$ Hz) LES C_{Mea} and empirical model C_{Mea} as a function of time during one cycle. Nominal configuration, $\mathrm{Re}_c = 77\,000$.

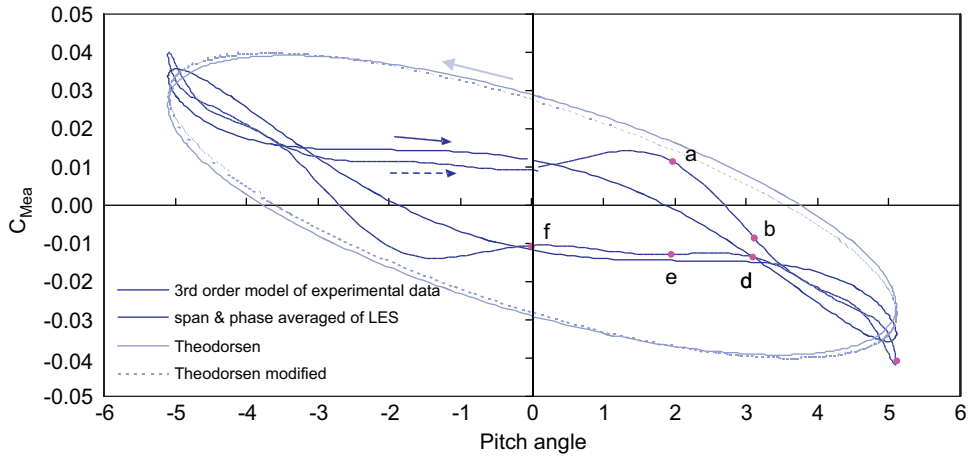

Fig. 23. Aerodynamic moment coefficient as a function of pitch angle during one cycle for (i) 3rd order empirical model of experimental results, (ii) span- and phase-averaged filtered ($f_c = 25$ Hz) LES, (iii) unsteady linear thin-airfoil aerodynamics theory and (iv) unsteady linear aerodynamics theory modified to account for airfoil thickness. Nominal configuration, $\mathrm{Re}_c = 77\,000$.

where over 20k time averages have been taken, as shown in Fig. 25 for different simulation models (Yuan et al., 2006). The corresponding pressure coefficient distribution is also shown. Moreover, for a NACA 0012 at $\mathrm{Re} = 10^5$ and $\alpha = 4^\circ$, DNS simulations (Shan et al., 2005) with over 240k time steps predicted a similar time-averaged behaviour with a positive local maximum of the C_f within the LSB. In this work, the criterion used to define the re-attachment point is where the friction coefficient becomes positive and stays positive, as shown for phase d in Fig. 24.

There is a notable exception, however, at $\alpha = 0^\circ$ (phase f). The skin-friction coefficient around $x/c \approx 0.5$ on the upper surface is not negative even though it is very close to zero. Based on the conventional definition of the separation, it is not a real separation zone. In this context, we call that region the "low speed" or "dead air" zone. Actually, this dead-air zone plays the same role as a laminar separation bubble. It results in the flattened pressure plateau as shown in the corresponding C_p plot. This flattened pressure plateau contributes to a nose-down pitching moment, too. Transition, then "re-attachment" follows.

The location of the separation and re-attachment points are corroborated by the pressure coefficient and the Reynolds shear stress distribution. The latter provides an indication of the separated-shear-layer transition leading to a turbulent boundary layer re-attachment. The laminar-turbulent transition is an unsteady process, which occurs as a consequence of an instability developed in the laminar boundary layer. The transition point was not specified prior to

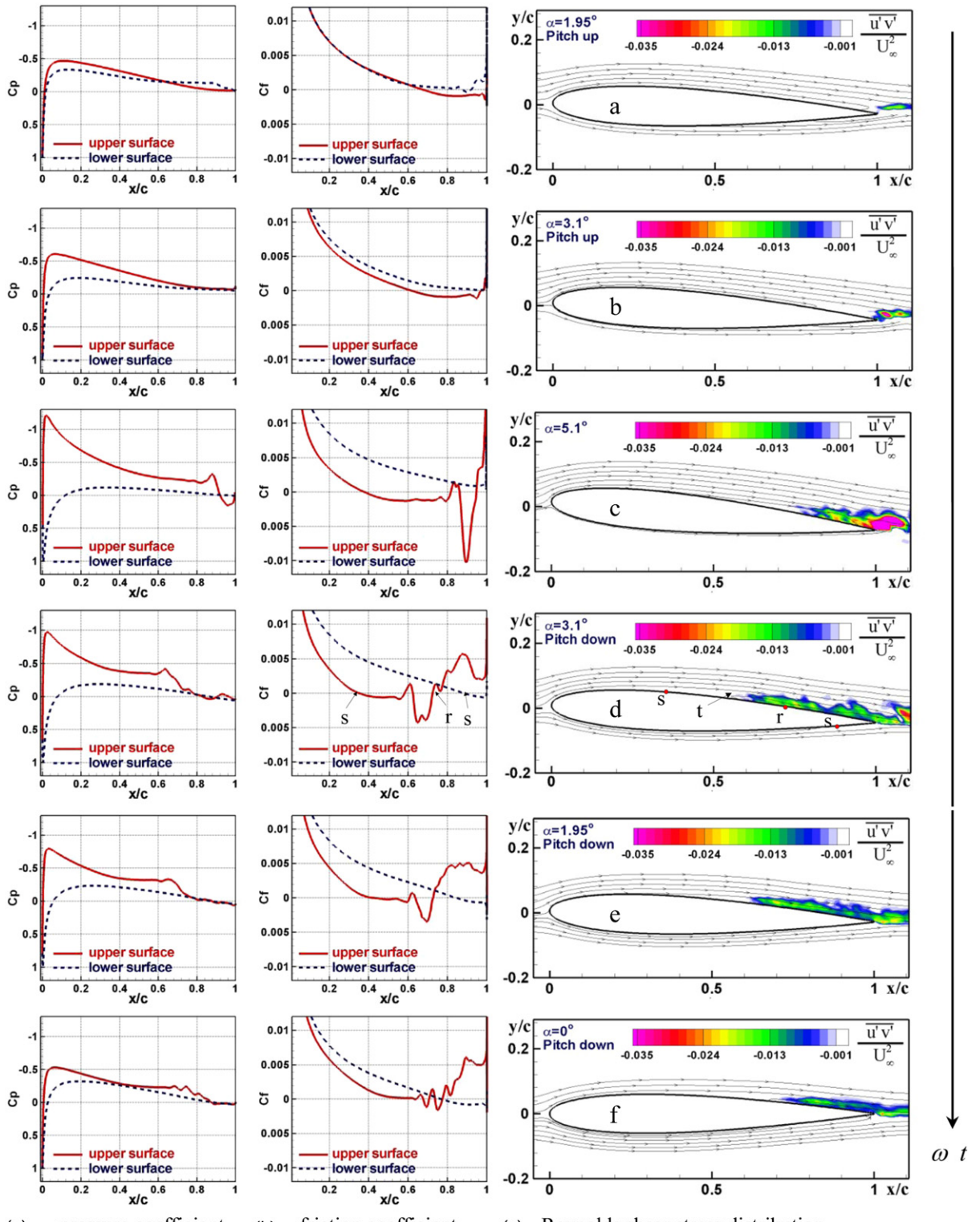

Fig. 24. C_p, C_f and Reynolds shear stress distribution, with initial separation (s), transition (t) and re-attachment (r) points shown for phase d. Span- and phase averages over 10 cycles of LES simulations. Nominal configuration, $Re_c = 77\,000$.

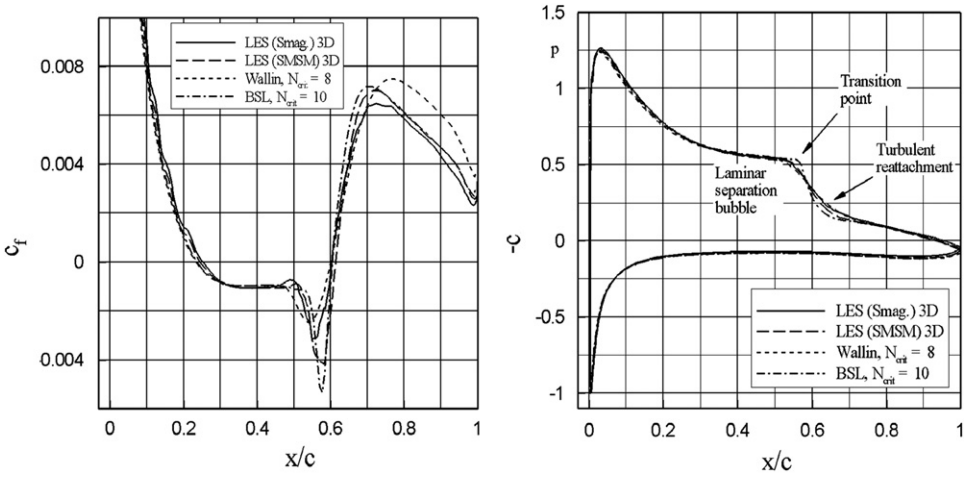

Fig. 25. Span- and time-averaged skin-friction coefficient (on the suction surface) and pressure coefficient distribution of a static SD7003 airfoil at $Re = 6.0 \times 10^4$ and $\alpha = 4^\circ$ (Yuan et al., 2006a).

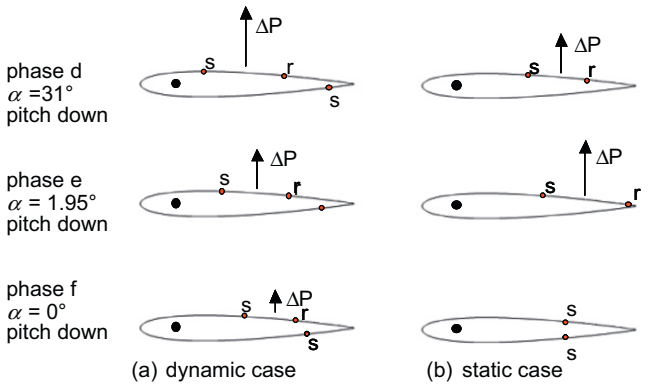

Fig. 26. Schematic of separation point (s) and re-attachment point (r) locations, and related moment–force, for phases d–f. Dynamic case on left-hand side; static case on right-hand side based on the work of Huang et al. (1996) work (suction side only for non-zero angles of attack).

the calculations but gathered from the Reynolds shear stress (i.e. $-\overline{u'v'}$) accumulated in the calculations. After the calculations, the $\overline{u'v'}$ distribution was obtained from statistical span and phase averaging. For attached flows, the boundary layer transition becomes most clearly detectable by a sudden and large increase in the boundary-layer thickness and in the shear stress near the wall, as well as in the decrease of the shape parameter (H). However, as applied in the RTO-AVT low-Reynolds aerodynamics research work (Arina et al., 2006) on the low-Re detached flows, the transition location is considered as the beginning of the turbulent wedge that starts spreading close to the separation streamline in the vicinity of the maximum thickness of the laminar separation bubble. In particular, for the sake of quantitative comparisons, the transition point was assumed to be located at the point where a value of $-\overline{u'v'}/U_\infty^2$ of 0.1% is reached and a clearly visible rise of the Reynolds shear stress is demonstrated. According to this criterion, the transition point is shown on Fig. 24 for phase d. Note that only the negative values of the Reynolds shear stress are presented, indicating momentum transport towards the airfoil upper surface.

The critical phases of the pitching cycle are from d to f. In this region the moment remains more or less constant, and negative, even though the pitch angle is decreasing from 3° to 0°. This flattening of the moment enables the formation of the clockwise inner loop near the origin, which is the source of the negative aerodynamic damping or similarly the time segment in the pitching cycle where the moment lags the pitch motion; see the discussion related to Figs. 22 and 23. Based on the flow field shown in Fig. 24, a schematic of the relevant physical features is presented in Fig. 26. Also shown on the right-hand side is the static counterpart as deduced from Huang et al.'s work (1996).

First looking at the dynamic case, as the wing pitches down from 3° to 0°, the decreasing length of the LSB (decreasing ΔP shown as a vector in the figure) is counterbalanced by a rearward motion of the LSB (which implies an increasing moment arm relative to the reference axis at $0.18c$). Thus, the (negative) pitch moment remains nearly unchanged.

In comparison with the static case, in the restricted range of angle of attack where the LSB exists, the separation point moves faster than the re-attachment point during pitch down (i.e. decreasing length of LSB) for the dynamic case whereas it moves slower than re-attachment (i.e. increasing length of LSB) for the static case. However, the comparison with the static case is most instructive at 0°. On both sides of the airfoil, the position of the laminar separation point, s, is delayed for the dynamic case. In other words, the separation points for the pitching airfoil are lagging the motion. Specifically, on the bottom side (pressure face), the separation point is moving forward but is behind its static case location. Since the separation region is associated with a local pressure reduction compared with the non-separated flow, the dynamic case has a smaller region of pressure reduction on the bottom side, thus resulting in a smaller pitch up moment, i.e. negative at this particular angle of attack compared with the static case. On the upper side (suction face), the separation point is moving backward but is ahead of its static case location. This also causes a nose down pitching moment, but which is somewhat mitigated by the re-attachment downstream. In summary, the lag between the pitching motion and the laminar separation points causes the negative aerodynamic damping and the appearance of the aeroelastic self-sustained oscillations, or flutter.

4. Conclusion

The aerodynamic moment of a NACA 0012 airfoil oscillating freely in pitch about a zero angle of attack has been investigated at $\mathrm{Re}_c = 77\,000$. This Reynolds number is in the transitional regime where complex viscous phenomena occur. The characteristics of the aeroelastic LCO are reminiscent of stall flutter except that they occur at small pre-stall angles and have shown a strong Re dependency in previous works. Using the restoring force surface method, in conjunction with a fitting procedure, an empirical model of the aerodynamic moment has been developed. The results of this analysis are consistent with published data, where available, and are compatible with the observed aeroelastic behaviour. It is shown that the aerodynamic stiffness is highly nonlinear and behaves like a softening spring in the range of angles of attack considered.

The origin of the oscillation is negative aerodynamic damping and it is physically related to the laminar trailing-edge separation, hence the name *laminar separation flutter* by analogy to stall flutter as well as to mark the difference between these two types of flutter. As the oscillations grow onto an LCO, the higher order aerodynamic moment damping terms become stronger and neutralize the dynamically destabilizing effect of the linear aerodynamic coefficient. It is speculated that these higher order terms are somehow physically related to the LSB. Furthermore, even though the pitch motion is nearly simple harmonic, the aerodynamic moment displays strong superharmonic content especially at three times the fundamental frequency. LES-based simulations of the flow, using a pure SHM pitch input, confirm the inherent odd super-harmonic content. They also highlight the significant contribution of the laminar separation and the related transition across the laminar separation bubble to the self-sustained oscillations of the airfoil observed in the experiments. Furthermore, the aerodynamic simulations corroborate the self-sustaining nature of the phenomenon since the work done by the flow over one cycle of pitch motion is positive and nearly equal to the one obtained experimentally.

Acknowledgments

The financial support of the Department of National Defence Canada (DND), through the ARP and AERAC programs, of the National Research Council of Canada (NRC) and of the Natural Sciences and Engineering Research Council of Canada (NSERC) are gratefully acknowledged. The first author would also like to thank Prof. A. Benaissa from RMC for fruitful discussions.

References

Arina, R., Atkin, C., Hanff, E., Jones, K., Lekas, T., Ol, M., Khalid, M., McAuliffe, B., Paquet, J.-B., Platzer, M., Radespiel, R., Rist, U., Windte, J., Yuan, W., 2006. AVT-101 final report: experimental and computational investigations in low Reynolds number aerodynamics, with applications to micro air vehicles. RTO Technical Report, NATO.

Bisplinghoff, R., Ashley, H., Halfman, R., 1983. In: Aeroelasticity. Dover Publications, Inc., Mineola, New York.

Collin, X., 2007. In: Étude de l'écoulement à Faibles Nombres de Reynolds Autour d'une aile en Oscillations Aéroélastiques Auto-Entretenues. Mémoire d'Ingénieur, Conservatoire National des Arts et Métiers, Toulouse, France.

Cebeci, T., Platzer, M., Chen, H., Chang, K.C., Shao, J.P., 2005. In: Analysis of Low-Speed Unsteady Airfoil Flows. Springer, Berlin.

Choi, H., Moin, P., Kim, J., 1993. Direct numerical simulation of turbulent flow over riblets. Journal of Fluid Mechanics 225, 503–539.

Davidson, L., Cokljat, D., Froehlich, J., Leschziner, M.A., Mellen, C., Rodi, W., 2003. In: LESFOIL: Large Eddy Simulation of Flow around a High Lift Airfoil. Springer-Verlag, Berlin.

Gad-el-Hak, M., 1990. Control of low-speed airfoil aerodynamics. AIAA Journal 28 (9), 1537–1552.

Huang, R.-F., Shy, W.W., Lin, S.W., Hsiao, F.-B., 1996. Influence of surface flow on aerodynamic loads of a cantilever wing. AIAA Journal 34 (3), 527–532.

Huang, R.-F., Lee, H.-W., 1999. Effects of freestream turbulence on wing-surface flow and aerodynamic performance. Journal of Aircraft 36 (6), 965–972.

Huang, R.-F., Lin, C., 1995. Vortex shedding and shear-layer instability of wing at low-Reynolds numbers. AIAA Journal 33 (8), 1398–1403.

Khalil, M., Poirel, D., Sarkar, A., 2009. Parameter estimation of stochastic aeroelastic systems from wind tunnel data: a sequential data assimilation approach. In: Presented at the 10th US National Congress of Computational Mechanics, Columbus, OH, USA.

Lutz, Th., Würz, W., Wagner, S., 2001. Numerical optimization and wind-tunnel testing of low Reynolds number airfoils, in fixed and flapping wing aerodynamics for micro air vehicle applications. In: Mueller, T.J. (Ed.), Progress in Astronautics and Aeronautics, vol. 195. AIAA, Reston, pp. 169–190.

Lund, T.S., Kaltenbach, H.-J., Akselvoll, K., 1995. On the behaviour of centered finite difference schemes for large eddy simulation. In: Proceedings of the Sixth International Symposium on Computational Fluid Dynamics, Lake Tahoe, USA.

Mueller, T.J., 1985. Low Reynolds Number Vehicles, AGARD-AG-288.

Mary, I., Sagaut, P., 2002. Large eddy simulation of flow around an airfoil near stall. AIAA Journal 40 (6), 1139–1145.

Mellen, C.P., Froehlich, J., Rodi, W., 2003. Lessons from LESFOIL project on large-eddy simulation of flow around an airfoil. AIAA Journal 41, 573–581.

Poirel, D., Harris, Y., 2005. Low frequency aeroelastic oscillations at low Re numbers. In: Proceedings of the 20th Canadian Congress of Applied Mechanics, Montreal, QC, Canada.

Poirel, D., Harris, Y., Benaissa, A., 2006. Aeroelastic dynamics of a NACA 0012 airfoil in the transitional Reynolds number regime. In: Proceedings of the Summer Conference of the ASME Pressure Vesssels and Piping Division, Vancouver, BC, Canada.

Poirel, D., Harris, Y., Benaissa, A., 2008. Self-sustained aeroelastic oscillations of a NACA 0012 airfoil at low-to-moderate Reynolds numbers. Journal of Fluids and Structures 24 (5), 700–719.

Runyan, H., 1951. Single-degree-of-freedom-flutter calculations for a wing in subsonic potential flow and comparison with an experiment. NACA TN 2396.

Shan, H., Jiang, L., Liu, C., 2005. Direct numerical simulation of flow separation around a NACA 0012 airfoil. Computers and Fluids 34, 1096–1114.

Voß, R., Wegner, W., 1992. Comparison of Euler and full potential methods for unsteady transonic flow calculations. In: AGARD Conference Proceedings 507 on Transonic Unsteady Aerodynamics and Aeroelasticity, pp. 8.1–8.17.

Worden, K., Tomlinson, G.R., 2001. In: Nonlinearity in Structural Dynamics. Institute of Physics Publishing, London.

Yuan, W., Khalid, M., 2004. Computation of unsteady flows past aircraft wings at low Reynolds numbers. Canadian Aeronautics and Space Journal 50 (4), 261–271.

Yuan, W., Khalid, M., Windte, J., Scholz, U., Radespiel, R., 2007a. Computational and experimental investigations of low-Reynolds-number flows past an airfoil. Aeronautical Journal 111 (1115), 17–29.

Yuan, W., Xu, H., Khalid, M., Radespiel, R., 2006. A parametric study of LES on laminar-turbulent transitional flows past an airfoil. International Journal of Fluid Dynamics 20 (1), 45–54.

Yuan, W., Khalid, M., Poirel, D., Benaissa, A., 2007b. Low-Reynolds-number effects on airfoil oscillations. In: Proceedings of the 25th AIAA Applied Aerodynamics Conference, Miami, AIAA-2007-4555.

Yuan, W., Khalid, M., Poirel, D., Benaissa, A., 2008. LES Investigations of Airfoil Oscillations at Low Reynolds Numbers, vol. 2. Institute for Aerospace Research, National Research Council Canada LTR-AL-2008-0073.